

# Non-parabolicity, band gap re-normalisation and carrier scattering in Si doped ZnO

R. E. Treharne<sup>a,\*</sup>, L. J. Phillips<sup>a</sup>, K. Durose<sup>a</sup>, A. D. Weerakkody<sup>b</sup>, I. Z. Mitrovic<sup>b</sup>, S. Hall<sup>b</sup>

<sup>a</sup>*Stephenson Institute for Renewable Energy, University of Liverpool, UK*

<sup>b</sup>*Department of Electrical Eng. and Electronics, University of Liverpool, UK*

---

## Abstract

test test test

*Keywords:* zinc oxide, magnetron sputtering, thin-film, doping, non-parabolicity, band gap normalisation

---

## 1. Introduction

Polycrystalline ZnO films have received significant attention in recent years. They can be degenerately doped by incorporating group III (e.g. Al, Ga or In [1]) or group VII (e.g. F [2, 3], Cl [4]) elements to achieve resistivities of the order  $10^{-4}$   $\Omega$ .cm while maintaining a high optical transparency, > 80%. Such ZnO based transparent conducting oxide (TCO) films, most notably Al doped ZnO (AZO), are now used extensively within thin-film photovoltaic technologies (namely CIGS, CZTS and CdTe) and have widely replaced the use of indium based TCOs. A wide range of deposition techniques have been demonstrated for ZnO films including atomic layer deposition (ALD) [5], metal-organic chemical vapour deposition (MOCVD) [6], pulsed laser deposition (PLD) [7] and magnetron sputtering [1, 8, 9].

The key properties of a TCO is its resistivity which is The most common approach to minimising a TCO's resistivity, with respect to any experimental parameter (e.g. pressure, temperature, composition), is to generate large

---

\*Corresponding author

Email address: R.Treharne@liverpool.ac.uk (R. E. Treharne)

sample sets over which a single parameter is varied incrementally. Such investigations are time consuming and the experimental consistency between each sample within a set can be poor due to random errors (e.g. drifts in other deposition parameters between samples). Furthermore, even for large sample sets the relationship determined between the resultant film properties and the deposition conditions can often be ambiguous.

## 2. Experimental Methods

Films were deposited via RF magnetron sputtering using an AJA Phase II-J Orion system. The system was configured in a 'sputter-up' geometry with the substrate being suspended above two separate ceramic targets of ZnO and SiO<sub>2</sub> arranged off-centre and tilted at 5° towards the centre of the substrate. Soda-lime glass substrates (OptiWhite<sup>TM</sup>, NSG Pilkington) of size 100 × 100 × 4 mm<sup>3</sup> were cleaned by scrubbing with a nylon brush and a series of de-ionized water and isopropanol alcohol rinses followed by blow drying with a nitrogen gas jet. During deposition the ZnO and SiO<sub>2</sub> targets were sputtered from simultaneously using powers of 150 W and 50 W respectively. A growth pressure of 2.7 × 10<sup>-3</sup> mbar Ar was used during deposition. The substrate temperature was maintained at 350 ± 5°C during growth and the substrate was kept static with respect to the magnetrons (i.e the substrate was not rotated). Deliberate gradients of both thickness and composition were subsequently achieved across the resultant film to generate a 'combinatorial' sample. A second film of pure SiO<sub>2</sub> was deposited under identical conditions (but without ZnO) to generate a reference film for estimating the % wt. profile of SiO<sub>2</sub> in the co-sputtered combinatorial sample.

A Shimadzu UV-Vis-IR 3700 spectrophotometer with mapping capability was used to measure the transmittance of the co-sputtered film over the range 250 - 2500 nm. 289 spectra were taken in total at 5 mm increments over the full sample surface. At each of these 289 points the sheet resistance was also measured using a CMT-SR2000 4-point probe mapping system. Following transmittance and sheet resistance measurements the sample was cut into one hundred

45  $10 \times 10 \text{ mm}^2$  pieces. A selection of these pieces, 10 in total, were further scribed  
 46 into four  $5 \times 5 \text{ mm}^2$  sections and Hall measurement were performed on each  
 47 of these sections. Hall measurements were performed with custom built equip-  
 48 ment, provided by Semimetrics Ltd., using a field strength of 0.8 T. Ellipsometry  
 49 was performed on the same sections using a Woollam M2000-UI system. Ellip-  
 50 sometry was also used to map the thickness profile of the pure  $\text{SiO}_2$  reference  
 51 film.

### 52 **3. Results**

#### 53 *3.1. Fitting of optical spectra*

54 Figure 1 shows a typical transmittance spectra taken from a single point  
 55 on the combinatorial ZnO:Si sample and the corresponding fit achieved using  
 56 a theoretical model of the material's dielectric permittivity  $\varepsilon(\omega)$ . Full details  
 57 of this model are given in [10]. The key components of the model include:  
 58 1) a Lorentzian oscillator to account for the behaviour of the system's bound  
 59 electrons and to provide a smoothly varying dielectric background over the range  
 60 of interest (250–2500 nm), 2) an extended Drude model [11], to characterise the  
 61 system's free electron response, and 3) an inter-band transition model to account  
 62 for the steep increase in the material's absorption coefficient ( $\alpha \propto (E - E_G)^{1/2}$ )  
 63 in the vicinity of its direct band gap (3.3 – 3.4 eV). The two key parameters  
 64 extractable from the dielectric model are the film's thickness,  $d$ , and plasma  
 65 frequency,  $\omega_p$ , which is related directly to the carrier concentration according  
 66 to

$$\omega_p = \sqrt{\frac{n_e e^2}{m_e \varepsilon_\infty \varepsilon_0}} \quad (1)$$

67 where  $m_e$  is the effective electrons (expressed in units of the free electron mass,  
 68  $m_0$ ),  $\varepsilon_\infty$  is the material's high frequency relativity permittivity ( $\sim 8.3$  for single  
 69 crystal ZnO [12]) and  $\varepsilon_0$  is the permittivity of free space. The optical dispersion  
 70 for the material, i.e. refractive index  $n$  and extinction coefficient  $\kappa$  are also  
 71 extracted from the fitting procedure and are shown in the inset of figure 1.

72 Fitting was achieved by using a Nelder-Mead downhill simplex algorithm  
73 [13], implemented via python script, to minimize the quantity

$$\chi^2 = \sum_i^N \sqrt{\frac{y_i - O_i}{N^2}} \quad (2)$$

74 where  $N$  is the total number of data points in the spectra,  $O_i$  the observed  
75 transmittance at each wavelength over the range of interest, and  $y_i$  the the-  
76 oretical transmittance calculated using the transfer matrix method [14] for a  
77 single thin-film on a finite, transparent substrate. The fitting algorithm was it-  
78 erated until the relative fractional change in consecutive  $\chi^2$  values was less than  
79  $1 \times 10^{-6}$ . The fitting of all 289 transmittance spectra taken over the combina-  
80 torial sample was fully automated, the only user input required being an initial  
81 estimate of film thickness at the point of the first spectrum. This automation  
82 ensured that the fitting of consecutive spectra was highly consistent. For all  
83 spectra,  $\chi^2$  values of  $< 1$  were achieved indicating that all fits were as successful  
84 as that shown in figure 1.

85 It was not possible to extract values for the true optical band-gap  $E_G$  from  
86 the inter-band transition component of the model. All values were typically  
87  $\sim 0.2$  eV lower than expected (even once non-parabolicity and re-normalisation  
88 effects had been accounted for, see sections 3.2 and 4). This is due to the pres-  
89 ence of a population of impurity states located in energy just below the bottom  
90 of the conduction band. The presence of these states generate a broadening,  
91 commonly referred to as an ‘Urbach tail’ [15], in the onset of the absorption  
92 coefficient. It is very difficult to determine the extent of this broadening by fit-  
93 ting the dielectric model to a single transmittance spectra. The use of variable  
94 angle spectroscopic ellipsometry (VASE) permitted the determinatin of the true  
95 band gap of the material as it only probed the interface of the films and did not  
96 sample the Urbach states.

97 For each point over the combinatorial sample ellipsometric spectra were  
98 taken at angles of 65 and 70° with respect to a plane normal to the sample  
99 surface. The spectra were and fitted using a parameterized semi-conductor  
100 (PSEMI-M0) model [16] over the range 350 – 1000 nm. Figure 2 shows a typical

101 fit achieved by the model and the inset shows the difference in the  $\alpha^2$  versus  
 102  $E$  behaviour extracted from transmittance and ellipsometry data respectively.  
 103 This disparity between band gaps extracted from the two techniques is in good  
 104 agreement with that reported previously by Srikant [17] in ZnO.

### 105 3.2. Conduction band non-parabolicity

106 For highly doped metal-oxides it has been shown that the conduction band,  
 107  $E_c$ , is ‘non-parabolic’ and that the origin of this non-parabolicity may be at-  
 108 tributed to a carrier dependent effective mass,  $m_e(n_e)$ . The functional form of  
 109 this dependence, first suggested by Pisarkiewicz *et. al* [18], is given by

$$m_e(n_e) = m_{e0} \sqrt{1 + \frac{2C\hbar^2 k}{m_{e0}}} \quad (3)$$

110 where  $m_{e0}$  is the value of the effective mass at the conduction band minimum  
 111 and  $C$  is the non-parabolicity factor, expressed in  $\text{eV}^{-1}$ . The carrier wave-  
 112 number can be expressed in terms of the carrier concentration according to  $k =$   
 113  $(3\pi^2 n_e)^{1/3}$ . By re-examining equation 1 it is clear that the relationship between  
 114  $\omega_p^2$  and  $n_e$  becomes non-linear if the effective mass is not a constant. Figure 3  
 115 shows a plot of  $\omega_p$ , extracted from the spectrophotometry measurements, versus  
 116 the carrier concentration,  $n_e^H$ , determined via Hall measurements, for the sample  
 117 subset cut from the original combinatorial sample. A similar  $\chi^2$  minimization  
 118 procedure to that described in section 3.1, in which the fitting parameters were  
 119  $m_{e0}$  and  $C$ , was applied to the data set using

$$\chi^2 = \sum_{i=1}^n \frac{(n_{e_i}^S - n_{e_i}^H)^2}{n^2} \quad (4)$$

120 where the superscript  $S$  corresponds to carrier concentrations calculated, us-  
 121 ing a carrier dependent effective mass  $m_e(n_e)$  (equations (1) a 3), from the  
 122 spectroscopically determined plasma frequencies. The superscript  $H$  denotes  
 123 values of  $n_e$  determined directly via Hall measurements. To determine the un-  
 124 certainty associated with the fitted  $m_{e0}$  and  $C$  values a Monte-Carlo style error  
 125 treatment [19] was implemented within which the  $\chi^2$  minimization procedure

was performed 1000 times. The inset plot in figure 3 shows the mean  $m_e(n_e)$  relationship (solid line) and the corresponding spread (yellow line). An average extracted value of  $m_{e0} = 0.35 \pm 0.02 m_0$  is higher than previous published values of  $0.24 - 0.28 m_0$  for the effective mass in undoped ZnO. An average extracted value of  $C = 0.30 \pm 0.01$  eV agrees very well with previously reported values of  $\sim 0.29$  eV<sup>-1</sup> [9, 20] for Al doped ZnO films.

### 3.3. Band-gap renormalization

The optical band gap of a degenerately doped metal-oxide system increases as a function of carrier concentration (Burstein-Moss shift [21, 22] according to

$$E_G = E_{G0} + \frac{\hbar^2(3\pi^2 n_e)^{2/3}}{2m_{eff}} \quad (5)$$

where  $E_{G0}$  is the band-gap at the conduction band minimum and the joint density of states effective mass,  $m_{eff}$  is given as

$$\frac{1}{m_{eff}} = \frac{1}{m_h} + \frac{1}{m_e(n_e)} \quad (6)$$

A constant hole effective mass value of  $m_h = 0.7 m_0$  [] is assumed throughout this work. Note that the non-parabolicity of the conduction band is accounted for when estimating the band gap by using the carrier dependent effective mass  $m_e(n_e)$  determined in section 3.2. The data points in figure 4 show the band-gap values, determined via ellipsometry, plotted against the Hall carrier concentrations. The points lie some distance from the relationship predicted by equation 5. The apparent reduction in the real band-gap values is due the renormalization effects of many body electron-electron, electron-ion and hole-hole interactions. Lu *et. al* [23] have shown that the total energy shift due to renormalization can be estimated by parameterising the detailed model described by Jain *et. al* [24, 25] according to

$$E_R = A n_e^{1/3} + B n_e^{1/4} + C n_e^{1/2} \quad (7)$$

where  $E_R$  is negative with respect to  $E_G$ . The  $n_e^{1/3}$ ,  $n_e^{1/4}$  and  $n_e^{1/2}$  dependencies correspond to the exchange energy of free electrons, their correlation energy

and the electron-ion interaction energy respectively. The coefficients  $A$ ,  $B$ , and  $C$ , quantify the strength of each of these three dependencies. The coefficient values for the data shown in figure 4, and a value for  $E_{G0}$ , was extracted using the established minimisation procedure. Table 1 show the extracted values and comparative values for n-type ZnO thin-films. The strength of the  $n_e^{1/3}$  dependence is roughly three times than that reported for Al doped ZnO.

#### 4. Mapping of compositional dependence

Film thickness profiles were determined for the combinatorial ZnO:Si and SiO<sub>2</sub> samples. The % wt. SiO<sub>2</sub> content at each point over the combinatorial sample was estimated according to

$$x = \frac{\Gamma_B d_B}{\Gamma_A d_A + \Gamma_B d_B} \times 100\% \quad (8)$$

where  $\Gamma_A$  and  $\Gamma_B$  are the bulk densities of ZnO and SiO<sub>2</sub> respectively and  $d_A$  and  $d_B$  are the corresponding thicknesses,  $d$ , of the ZnO and SiO<sub>2</sub> films. The carrier concentration profile for the combinatorial sample was calculated from extracted  $\omega_p^S$  values according to equation 1 and using the non-parabolic effective mass relationship,  $m_e(n_e)$ , determined in section 3.2. The corresponding mobility profile was calculated according to

$$\mu_e = \frac{1}{n_e^S R_S d_e} \quad (9)$$

where  $R_S$  are the sheet resistance values obtained directly from 4 point probe measurements. Figure 5 shows the three dimensional contour profiles of  $n_e$  and  $\mu_e$  accross the surface of the combinatorial sample. In both cases, a maximal ridge, corresponding to  $n_e \sim 4.5 \text{ cm}^{-3}$  and  $\mu_e \sim 16 \text{ cm}^2 \text{V}^{-1} \text{s}^{-1}$ , runs diagonally across the sample. By superimposing the contour distribution of % wt. SiO<sub>2</sub> content (dotted black contour lines) a very strong correlation between carrier concentration and composition becomes apparent, the maximum  $n_e$  and  $\mu_e$  values corresponding to a value of  $x = 0.65\%$  wt. SiO<sub>2</sub> content.

By plotting the distributions of  $n_e$  and  $\mu_e$  with respect to  $x$  the compositional dependence can be observed directly, see figure 6. Here the strength of the

combinatorial analysis is fully appreciated by its ability to generate continuous, non-ambiguous distributions of the material's electrical behaviour and shows that it is highly sensitive to the composition - the resistivity spanning over three orders of magnitude within the compositional range  $x = 0 - 0.65\%$  wt.  $\text{SiO}_2$ . Furthermore, the uncertainty in the optimum value of  $x$ , that minimises the resistivity, is significantly reduced when compared to the multi-sample analyses that are commonly reported.

The solid straight line in the  $n_e$  vs  $x$  plot indicates the relationship predicted for a 100% doping efficiency, i.e. where every Si atom incorporated into film substitutionally replace a Zn atom and contributes two free electrons to the system. For low values of  $x$ , i.e. in the range  $0 - 0.5\%$  wt.  $\text{SiO}_2$ , this relationship is adhered to. However as  $x$  increases further the doping efficiency decreases rapidly and the carrier concentration is limited to  $3 - 4 \times 10 \text{ cm}^{-3}$  for compositions up to  $10\%$  wt.  $\text{SiO}_2$ . After the optimum value of  $x$  is reached the mobility drops off steeply and approaches a value of zero for values of  $x$  beyond  $6\%$ . This suggests that as  $x$  is increased beyond the optimum composition, Si is no longer incorporated into the film as a substitutional dopant and instead acts to increase the scattering of the free carriers, existing as an interstitial impurities or forming segregated Si-O phases at the grain boundaries.

#### 4.1. Scattering

The behaviour of carrier mobility can be described further by considering its direct relationship with the carrier concentration. Figure 5 shows that by plotting  $\mu_e$  versus  $n_e$  for all data points two distinct populations are revealed. The red data points correspond to compositions  $x < 0.65\%$ . Within this distribution, and for carrier concentrations below  $2.5 \times 10 \text{ cm}^{-3}$  the mobility of the free carriers can be described in terms of a grain barrier limited transport model proposed by Seto *et.al* [26]. The model assumes that at the grain boundaries a population of filled trap states exist within the band gap. This causes the conduction band to bend upwards at each grain boundary forming a barrier to charge transport. The inter-grain mobility,  $\mu_B$  of free carriers is therefore



206 limited by thermal processes according to

$$\mu_{ig} = \mu_0 \exp\left(-\frac{\Phi_B}{k_B T}\right) \quad (10)$$

207 where  $\Phi_B$  is the barrier height at the grain boundary and is related directly to  
208 the carrier concentration according to

$$\Phi_B = \frac{e^2 n_t}{8\varepsilon_\infty \varepsilon_0 n_e} \quad (11)$$

209 where  $n_t$  is the trap density and  $\varepsilon_\infty$  is the high frequency dielectric permittivity  
210 ( $\varepsilon_\infty \sim 8.3$  for single crystal ZnO [12]). The pre-factor  $\mu_0$  is the internal mobility  
211 of the grain, expressed as

$$\mu_0 = \frac{eL}{\sqrt{2\pi m_e k_B T}} \quad (12)$$

212 where  $L$  is the grain size. It is necessary to extend the Seto model in the case  
213 of degenerately doped ZnO to account for the tunnelling of carriers through the  
214 barrier  $\Phi_B$ . As the carrier concentration increases the Fermi level rises towards  
215 the top of the barrier while the barrier height decreases proportionally to  $1/n_e$ .  
216 Following the onset of tunnelling the effective carrier mobility increases expo-  
217 nentially with respect to carrier concentration. The mobility and is eventually  
218 limited by other scattering processes, for example ionized-impurity scattering.  
219 A semi-empirical relationship the mobility due to the tunnelling of free carriers  
220 ,  $\mu_t$  can be expressed according to

$$\mu_t = \frac{\mu_{ii} - \mu_{ig}}{1 + \exp\left[-\frac{1}{\alpha}(\Delta_{BM} + E_R - \beta\Phi_B)\right]} \quad (13)$$

221 where the factor  $\alpha$  accounts for the sharpness of the onset in tunnelling and  
222 is likely to be related to the depletion width of the grain boundary. A second  
223 empirical factor,  $\beta$  takes into account of any extra functional dependence of  $\Phi_B$   
224 on  $n_t$  which is likely vary with respect to  $n_e$ . The effective mobility may therefore  
225 be expressed as the sum of the inter-grain and tunnel mobilities according to

$$\mu_{eff} = \mu_{ig} + \mu_t \quad (14)$$

226 Figure 5 shows corresponding the fit of this extended model to the data in the  
227 region of composition  $x < 0.65\%$ . An extracted value of  $n_t = 1.79 \times 10^{14} \text{ cm}^{-3}$  is

over two orders of magnitude greater than that reported for reactively sputtered, undoped ZnO films [27] and an order of magnitude greater than that for Al doped ZnO films [28]. This is reflected in the relatively low optimum mobility values of  $\sim 16 \text{ cm}^2\text{V}^{-1}\text{s}^{-1}$  which is typically half that of Al doped ZnO films. The reduction of the level trap densities at the grain boundaries is therefore key to the improvement of carrier mobility in Si doped ZnO films. This is likely to be achieved through further investigations of the effect of growth parameters, i.e. substrate temperature and sputter pressure. Based on the model used in this work, a reduction of  $n_t$  by  $\sim 20\%$  could yield a doubling of the mobility.

The green data points in figure 5 show the  $n_e$  versus  $\mu_e$  behaviour for  $> 0.65\%$  wt.  $\text{SiO}_2$  compositions. The mobility now tends towards a minimum value at a higher carrier concentration of  $\sim 3 \text{ cm}^2\text{V}^{-1}\text{s}^{-1}$ . This is indicative of an increased trap density, the result of an excess of Si at the grain boundaries or perhaps the formation of Si-O phases.

## 5. Conclusions

A consideration of the non-parabolicity of the conduction band for Si doped ZnO has yielded estimates for the values of the band minimum effective mass,  $m_{e0} = 0.35m_0$ , and the non-parabolicity factor,  $C = 0.3 \text{ eV}^{-1}$ . The non-parabolicity contributes to a reduction in the expected Burstein-Moss shift of the optical band-gap at carrier concentrations beyond  $10^{20} \text{ cm}^{-3}$ . Further reductions in the band-gap arises from the renormalization effects which are dominated by electron-electron and electron-ion interactions. For Si doped films the component of the magnitude of these effects are significantly greater than that reported for sputtered Al doped ZnO films.

The combinatorial methodology employed within this work allows the relationship between composition and the electrical behaviour to be determined with excellent accuracy, with a continuous distributions between  $n_e$ ,  $\mu_e$ ,  $\rho$  and  $\%$  wt.  $\text{SiO}_2$  being determined. Furthermore, the extraction of all data from a single sample ensures that a high level of consistency between each data point

is achieved compared with measurements taken over a series of separately deposited samples. Maximum values of  $4.5 \times 10^{20} \text{ cm}^{-3}$  and  $16 \text{ cm}^2\text{V}^{-1}\text{s}^{-1}$  were achieved for the carrier concentration and mobility respectively, at an optimal composition of  $x = 0.65\%$  wt.  $\text{SiO}_2$ , and this corresponding to a minimum resistivity of  $8.7 \text{ }\Omega\cdot\text{cm}$ .

The model of grain boundary scattering proposed by *Seto* [26] has been extended to include the effects of tunneling through grain boundaries. The model generates a good agreement for the observed  $\mu_e$  versus  $n_e$  behaviour at compositions up to the optimum value of  $x$ . The model highlights a potential route to improving carrier mobility, i.e. by reducing the density of trap states that exist at the grain boundaries.

Above the optimum composition a different dependence is observed to that below it. This is thought to be due to the increased density of trap states associated with the incorporation of excess Si into the films.

- [1] T. Minami, *Semicond. Sci. Technol.* 20 (2005) S35.
- [2] J. Hu, R. Gordon, *Solar Cells* 30 (1991) 437–450.
- [3] R. E. Treharne, K. Durose, *Thin Solid Films* 519 (2010) 7579–7582.
- [4] J. Rousset, E. Saucedo, D. Lincot, *Chem. Mater.* 21 (2009) 534–540.
- [5] P. R. Chalker, P. A. Marshall, S. Romani, J. Roberts, W. Joseph, S. J. C. Irvine, D. Lamb, A. Clayton, J. Andrew, P. A. Williams, *J. Vac. Sci. Technol. A* 31 (2012) 01A120–01A120.
- [6] S. Y. Myong, S. J. Baik, C. H. Lee, W. Y. Cho, K. S. Lim, *Jpn. J. App. Phys.* 36 (1997) L1078.
- [7] S.-M. Park, T. Ikegami, K. Ebihara, S.-M. Shin, Paik-Kyun Park, T. Ikegami, K. Ebihara, P.-K. Shin, *App. Surf. Sci.* 253 (2006) 1522–1527.
- [8] T. Minami, T. Miyata, Y. Ohtani, Y. Mochizuki, *Jpn. J. App. Phys.* 45 (2006) L409–L412.

- 284 [9] K. Ellmer, J. Phys. D: Appl. Phys 34 (2001) 3097–3108.
- 285 [10] R. E. Treharne, K. Hutchings, D. A. Lamb, S. J. C. Irvine, D. Lane,  
286 K. Durose, J. Phys. D: Appl. Phys 45 (2012) 335102.
- 287 [11] D. Mergel, Z. Qiao, J. Phys. D: Appl. Phys 35 (2002) 794.
- 288 [12] N. Ashkenov, B. N. Mbenkum, C. Bundesmann, V. Riede, M. Lorenz,  
289 D. Spemann, E. M. Kaidashev, A. Kasic, M. Schubert, M. Grundmann, J.  
290 Appl. Phys. 93 (2003) 126–133.
- 291 [13] J. A. Nelder, R. Mead, The Computer Journal 7 (1965) 308–313.
- 292 [14] H. A. Macleod, Thin-Film Optical Filters, Adam Hilger Ltd, 1986.
- 293 [15] Urbach (????).
- 294 [16] C. Herzinger, B. Johs, W. McGahan, J. Woollam, W. Paulson, Journal of  
295 Applied Physics 83 (1998) 3323–3336.
- 296 [17] V. Srikant, D. R. Clarke, J. Appl. Phys. 83 (1998) 5447–5451.
- 297 [18] T. Pisarkiewicz, A. Kolodziej, Phys. Stat. Sol. B 158 (1990) K5–K8.
- 298 [19] R. J. Mendelsberg, Photoluminescence of ZnO grown by eclipse pulsed laser  
299 deposition, Ph.D. thesis, University of Canterbury, New Zealand, 2009.
- 300 [20] F. Ruske, A. Pflug, V. Sittinger, B. Szyszka, D. Greiner, B. Rech (????).  
301 Article in press - Thin Solid Films.
- 302 [21] E. Burstein, Physical Review 93 (1954) 632–633.
- 303 [22] T. S. Moss, Proceedings of the Physical Society. Section B 67 (1954) 775.
- 304 [23] J. Lu, S. Fujita, T. Kawaharamura, H. Nishinaka, Y. Kamada, T. Ohshima,  
305 Z. Ye, Y. Zeng, Y. Zhang, L. Zhu, et al., J. Appl. Phys. 101 (2007) 083705–  
306 083705.
- 307 [24] S. Jain, J. McGregor, D. Roulston, Journal of applied physics 68 (1990)  
308 3747–3749.

- 309 [25] S. C. Jain, D. J. Roulston, Sol. State. Elec. 34 (1991) 453–465.
- 310 [26] J. Y. W. Seto, J. Appl. Phys. 46 (1975) 5247–5254.
- 311 [27] P. F. Carcia, R. S. McLean, M. H. Reilly, G. Nunes, App. Phys. Lett. 82  
312 (2003) 1117–1119.
- 313 [28] M. Kon, P. Song, Y. Shigesato, P. Frach, S. Ohno, K. Suzuki, Jpn. J. App.  
314 Phys. 42 (2003) 263–269.
- 315 [29] B. Johs, J. A. Woollam, C. M. Herzinger, J. Hilfiker, R. Synowicki, C. L.  
316 Bungay, Crit. Rev. Opt. Sci. CR72 (1999) 29–58.
- 317 [30] R. J. Mendelsberg, Y. Zhu, A. Anders, J. Phys. D: Appl. Phys 45 (2012)  
318 425302.

Parameter 1	Extracted Value	Copmparison [23]
$A (\times 10^{-8} \text{ eV.cm})$	$2.1 \pm 0.8$	0.69
$B (\times 10^{-7} \text{ eV.cm}^{3/2})$	$3.0 \pm 2.6$	1.6
$C (\times 10^{-7} \text{ eV.cm}^{3/4})$	$8.7 \pm 1.5$	7.76
$E_{G0} \text{ (eV)}$	$3.41 \pm 0.01$	-

Table 1:

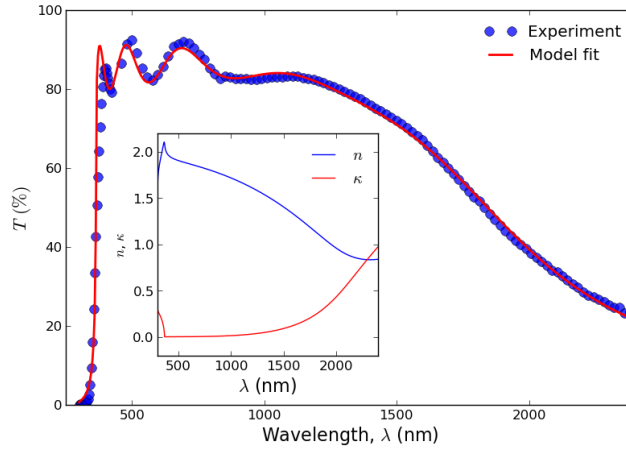


Figure 1: Example of a typical transmittance curve taken from a single point on the combinatorial ZnO:Si sample. The line (—) shows the corresponding fit generated by the dielectric model [10]. An excellent fit is achieved at wavelengths in the vicinity of plasma edge, i.e.  $> 1000$  nm. The band to band transition component of the model is insufficient to accurately describe the behaviour in the vicinity of the material's direct band gap. In this instance, values of  $d = 518 \pm 10$  nm,  $\varepsilon_{\infty}\omega_p = 0.97 \pm 0.02$  eV and  $E_G = 3.38 \pm 0.04$  eV were extracted from the fitting procedure. The inset also shows the dispersion relationships for  $n$  and  $\kappa$  extracted by the model.

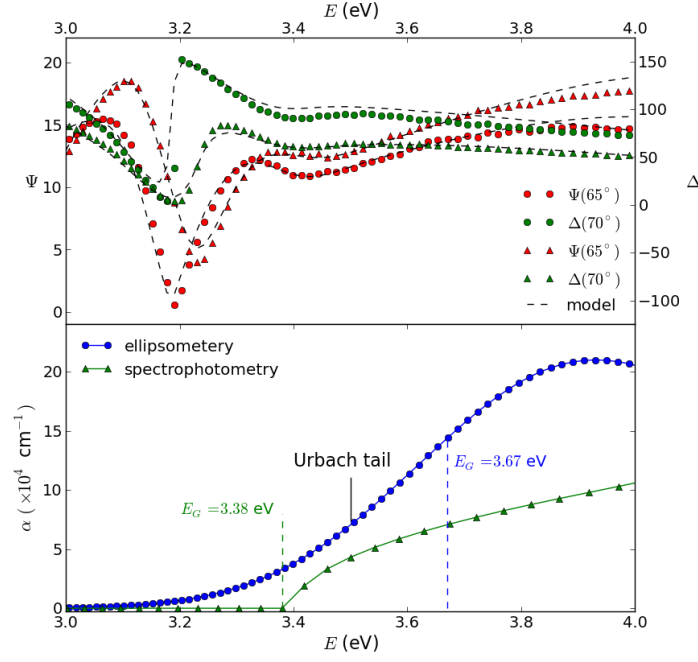


Figure 2: a) Ellipsometric spectra ( $\Psi$  and  $\Delta$ ), measured at separate angles of  $65^\circ$  and  $70^\circ$ , were fitted over the range 3 eV (413 nm) to 4 eV (309 nm) using a single PSEMI-MO oscillator [16, 29], b) The corresponding absorption coefficient extracted from the ellipsometric data compared with that extracted from the spectrophotometric data (1). A difference in the direct band gap of  $\sim 0.3$  eV is determined between the two optical extraction methods. The ellipsometric model is deemed to be more reliable due to its ability to account for the Urbach tail that arises from a distribution of impurity states located just below the bottom of the conduction band.

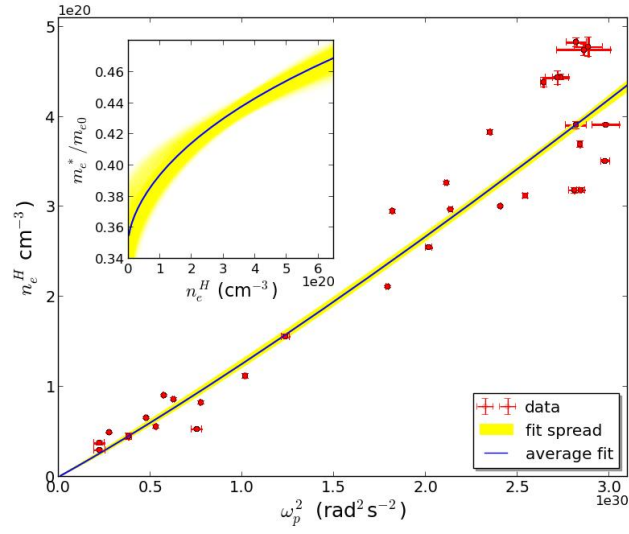


Figure 3: Carrier concentration,  $n_e^H$ , determined via Hall effect measurements versus values of  $(\epsilon_\infty \omega_p)^2$  extracted from the dielectric modeling of transmittance data. A Monte-Carlo style fitting procedure [19, 30] indicates that the relationship between the axes is non-linear, as expected for a material with a non-parabolic conduction band. The spread in uncertainty associated with the fitting procedure is shown by the yellow line. The corresponding relationship between the carrier effective mass,  $m_e$  and the carrier concentration is shown in the inset. Values of  $m_{e0} = 0.35 \pm 0.02 m_0$  and  $C = 0.30 \pm 0.01 \text{ eV}^{-1}$  were extracted from the analysis.



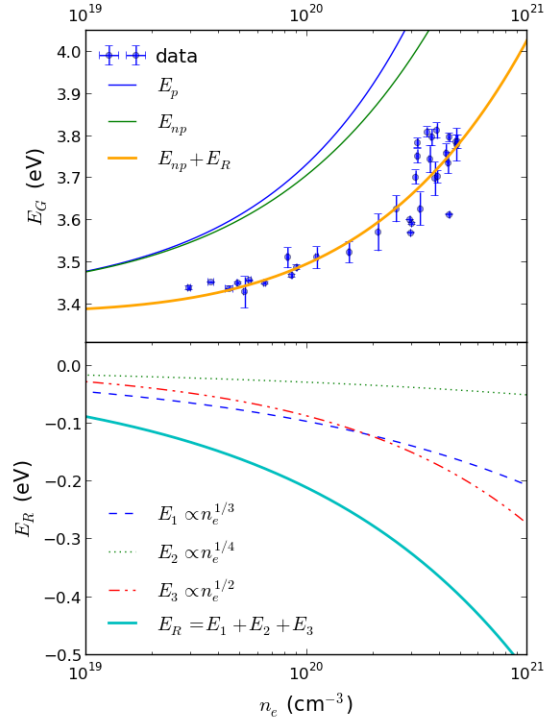


Figure 4: a) Ellipsometry extracted band gap values,  $E_G$ , plotted with respect to the carrier concentration determined by Hall measurements. The Burstein-Moss relation ( $E_p$ ), even once non-parabolicity is accounted for ( $E_{np}$ ), is insufficient to predict the observed relationship - band gap values being significantly lower than expected. The incorporation of renormalization effects permits the data to be fitted. b) The total renormalization energy and each of its subcomponents are shown. The amplitude of these components is calculated empirically via a Monte-Carlo fitting procedure using the model proposed by [24].

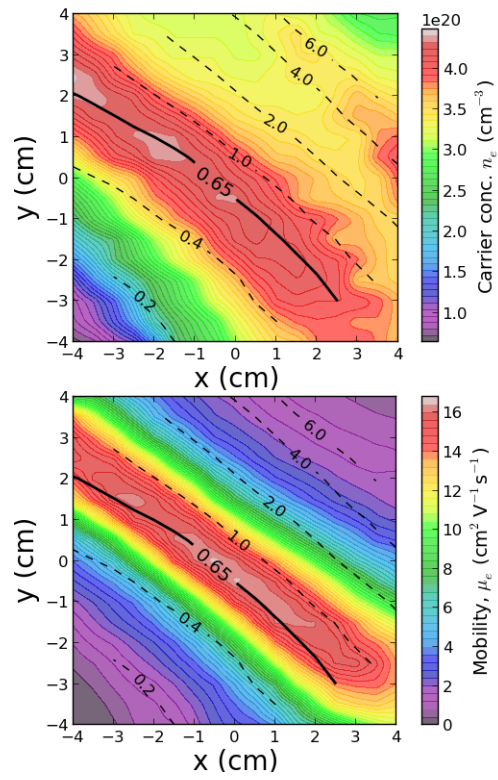


Figure 5: Contour maps of carrier concentration and mobility over the combinatorial sample. The ( - - ) contour lines show an overlay of the % wt.  $\text{SiO}_2$  composition.

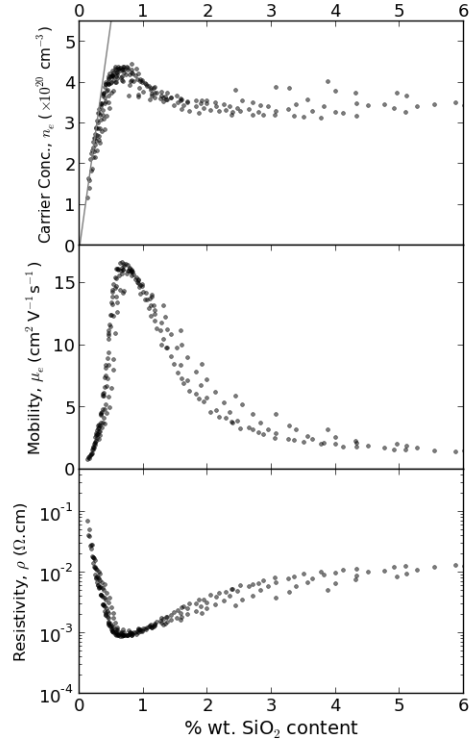


Figure 6: Distributions of carrier concentration, mobility and resistivity with respect to % wt.  $\text{SiO}_2$  content. The maximum values for  $n_e$  ( $4.4 \times 10^{20} \text{ cm}^{-3}$ ) and  $\mu_e$  ( $16.5 \text{ cm}^2 \text{V}^{-1} \text{s}^{-1}$ ) coincide with a composition of 0.65% wt.  $\text{SiO}_2$ . The solid straight line in the top plot shows the maximum theoretical carrier concentration with respect to  $\text{SiO}_2$  content should every incorporated Si atom be substituted at a Zinc site and donate 2 carriers.

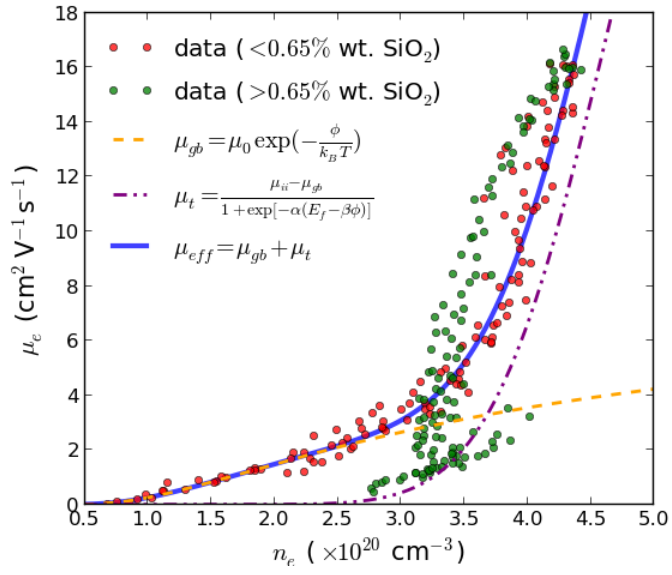


Figure 7: